



Cite this: *J. Mater. Chem. A*, 2025, **13**, 15871

Salt particle suspension electrolyte with trace-water for improving ionic concentrations at interfaces in zinc-based dual-ion batteries†

Yitao He, *^{ab} Fafa Yu^a and Jiří Červenka *^b

Dual-ion batteries (DIBs) have garnered significant interest due to their cost-effectiveness, high operating voltage, and eco-friendly nature. The electrolyte, serving as the provider of active ions during the charge/discharge cycles, is pivotal to the performance metrics of DIBs, such as capacity, energy density, and lifespan. Despite this, the high-concentration electrolytes that rely heavily on main salts often compromise the cost-effectiveness of DIBs. Therefore, a salt particle suspension electrolyte (SPSE) system has been successfully developed based on a linear carbonate solvent with a trace amount of water and applied in graphite||zinc and graphite||graphite DIBs. This innovative SPSE offers a high surface anion concentration that reduces concentration polarization, improves anion utilization efficiency at the electrode surface, and ensures a sufficient anion supply even at relatively low electrolyte concentrations. The prototype DIB, based on a zinc metal-free anode concept utilizing a graphite anode, an expanded graphite cathode, and a SPSE with a zinc trifluoromethylsulfonate [Zn(OTf)₂] salt has demonstrated a remarkable discharge capacity of 178.66 mA h g⁻¹ at a current rate of 10 mA g⁻¹, and an impressive 84.7% capacity retention after 240 cycles at 100 mA g⁻¹. The energy density of the battery with respect to the cathode mass soared to 304.8 W h kg⁻¹. Our results provide novel insight into the rational design and construction of superior suspension electrolytes for DIBs, demonstrating a groundbreaking electrolyte formulation strategy that can improve battery performance as well as lower production costs.

Received 10th January 2025
Accepted 8th April 2025

DOI: 10.1039/d5ta00256g

rsc.li/materials-a

1 Introduction

Dual-ion batteries (DIBs) are promising energy storage devices for large-scale energy storage applications. They can utilize both cations and anions in energy storage and combine different low-cost and environmentally benign materials, such as zinc anode and graphite cathode. They can also achieve a high operation voltage when using, for example, the intercalation/de-intercalation of anions into/out of the layered cathodes, such as graphite.^{1–4} As the electrolyte is the only source of active ions in DIBs, the electrolyte composition and concentration critically impact the battery performance, including capacity, energy density, and cycling life. However, the absence of anions in the cathode materials means that the electrolyte is the sole source of anions, creating a strong concentration gradient at the electrode surface.⁵ This condition can readily lead to the formation of concentration polarization during the battery charging

process. The management of concentration is pivotal in enhancing the electrochemical performance of DIBs.⁶ Therefore, much effort has been put into developing high-performance electrolytes.

Recently, researchers have begun to investigate “suspension electrolytes” made of slightly soluble salts.^{7–10} For example, Cui's group⁷ used the slightly soluble Li₂O nanoparticles contained in the SEI on the lithium metal as the additive in ester or ether electrolytes to form a suspension electrolyte and optimize the solvation structure, SEI composition and nucleation overpotential. The suspension electrolyte enhanced the coulombic efficiency of the lithium metal anode and cycle performance of the NCM811||Li full battery. Although this type of suspension electrolyte formed by inorganic additives has many interesting properties, it is not suitable for DIBs because the concentration of the main salt containing the intercalatable anions does not change. Moreover, the electrolyte could not alleviate the consumption of anions and cations in the DIBs during charging/discharging. Therefore, the suspension electrolyte must be further improved to meet the requirements of DIBs.

The hybrid solvent system of dimethyl carbonate (DMC) and water has attracted significant attention from battery researchers. For instance, Zhang's group¹¹ used Zn(OTf)₂ in a mixed solvent electrolyte when studying aqueous zinc-ion batteries. Their results showed that water molecules can

^aDepartment of New Energy Science and Engineering, School of Energy and Environment, Anhui University of Technology, Ma'anshan, China^bDepartment of Thin Films and Nanostructures, FZU – Institute of Physics of the Czech Academy of Sciences, Cukrovarnická 10/112, 162 00 Prague 6, Czech Republic. E-mail: yitao@fzu.cz; cervenka@fzu.cz† Electronic supplementary information (ESI) available. See DOI: <https://doi.org/10.1039/d5ta00256g>

regulate the solvation structure and facilitate the deposition of Zn^{2+} on the Zn metal anode and intercalation/de-intercalation of Zn^{2+} in the $\delta\text{-MnO}_2$ cathode. This solvent system can also be used in DIBs. For example, Xiao's group,¹² by introducing a DMC/water co-solvent, expanded the anodic limit of the electrolyte from 2.26 V (vs. Zn/Zn^{2+}) to 2.54 V and improved the average coulombic efficiency from 80% to 98%. The regulatory effect of DMC on the solvation structure enhanced the structural integrity of the graphite cathode and suppressed uneven zinc deposition and dendritic growth on the zinc anode. However, the graphite||Zn battery could only provide a low specific capacity of 40 mA h g^{-1} . Therefore, to fully leverage the potential and advantages of the DMC/water solvent system, there is a need to further modify the suspension electrolyte structure and enhance the specific capacity and energy density of DIBs.

This work utilizes the microsolubility of the main salt, zinc trifluoromethanesulfonate ($\text{Zn}(\text{OTf})_2$), in DMC to form solvated suspension particles, demonstrating a novel suspension electrolyte for high-performance DIBs. The electrolyte concentration only needs to be in the low concentration range of 1–3 M to facilitate excellent battery functions due to reduced concentration polarization and improved anion utilization efficiency. The solvated salt particles effectively replenish the ion concentration at the electrode surface, mitigating the concentration gradient during battery charging. Trace amounts of water are used solely as an additive to regulate the solvent structure of the anions and weaken the bond between the anion and the cation. The salt particle suspension electrolyte (SPSE) with the optimal trace amount of water has excellent fluidity, high charge/discharge voltage plateaus, and compatibility with the Zn metal or natural graphite anode and expanded graphite cathode, delivering excellent battery performance and an energy density of 304.8 W h kg^{-1} . Unlike previous suspension electrolytes that rely on additives or unable to sustain anion availability, the SPSE utilizes the controlled microsolubility of $\text{Zn}(\text{OTf})_2$ to continuously replenish anions, reducing concentration polarization and improving ion transport. This advancement enhances electrolyte efficiency and stability, making SPSE a promising solution for high-performance DIBs. It also demonstrates favorable compatibility with battery fabrication under atmospheric conditions, which is beneficial for low-cost manufacturing industrial processes and large-scale energy storage applications.

2 Experimental section

2.1 Materials

Pristine expanded graphite (1000 mesh) was purchased from the Nanjing Geruifa Carbon Materials Co., Ltd. The same results were obtained for zinc trifluoromethanesulfonate ($\text{Zn}(\text{OTf})_2$, 98%) purchased from two different manufacturers (Sigma-Aldrich, Shanghai, China; Benze reagent, China). Dimethyl carbonate (DMC) and *N*-methylpyrrolidone (NMP) were purchased from Aladdin. A stainless steel mesh (250 mesh), NKK-MPF30AC-100 separator (30 μm), carbon black (Super P), and polytetrafluoroethylene (PTFE) and CR2032 coin

cell cases were purchased from Kelude and Lizhiyuan, China. A graphite negative electrode (natural graphite sheet on Cu foil) was purchased from MTI, China. The Zn foil (99.995%, 10 μm) was purchased from Bosheng Metal Materials.

2.2 Positive electrode preparation

The pristine expanded graphite (EG) was ground carefully to a fine powder with a mortar and then annealed at 800 $^{\circ}\text{C}$ for 2 h in an Ar atmosphere. Typically, 80 wt% EG as the active material, 10 wt% Super P (as conductive carbon), and 10 wt% PTFE (as a binder) were mixed together using a stirrer in NMP solvent for 24 h. The slurry mixture was cast onto a stainless steel mesh and then temporarily dried at 60 $^{\circ}\text{C}$ for 20 min. The undried electrode laminates were compacted using a roll-pressing machine at 10 MPa. Subsequently, the undried compacted electrode laminates were dried at 60 $^{\circ}\text{C}$ for 10 h in a vacuum. The mass loading of active materials on the positive electrode laminates was around 0.65 mg cm^{-2} . All preparation steps were conducted under atmospheric conditions.

2.3 Solvated particle suspension electrolyte preparation

The DMC solvent was dehydrated by using a 3 Å molecular sieve. The $\text{Zn}(\text{OTf})_2$ powder was dried at 80 $^{\circ}\text{C}$ overnight in a vacuum to dehydrate and then added to the DMC solvent to prepare 1 M, 2 M and 3 M electrolytes. The solvation structure was optimized by directly adding trace amounts of water (15, 30, and 45 $\mu\text{L mL}^{-1}$) according to the $\text{Zn}^{2+}/\text{H}_2\text{O}$ molar ratio of 1:1. The solution was then placed on a magnetic stirrer for continuous stirring for 48 h and used immediately after stirring.

2.4 Material characterization

The morphology/microstructure and chemical composition of the samples were characterized by Field-emission scanning electron microscopy (FESEM, Merlin Compact, Zeiss, Germany) and X-ray photoelectron spectrometry (XPS, 250Xi, Thermo Scientific, USA). Raman spectra were obtained with a Renishaw micro-Raman spectroscopy system *via* a TE air-cooled 576 \times 400 CCD array utilizing a laser (532 nm) as the exciting source. The thermogravimetric analysis was performed using a DTG-60H thermogravimetric analyzer in a nitrogen atmosphere, and the temperature was increased from 30 to 400 $^{\circ}\text{C}$ at a heating rate of 10 $^{\circ}\text{C min}^{-1}$. *In situ* observations were made using an ordinary optical microscope with a 400 \times eyepiece.

2.5 Electrochemical measurements and battery testing

All CR2032 coin cells were assembled under atmospheric conditions (20–23 $^{\circ}\text{C}$ and 50–60% RH in our laboratory). A CHI760E Analytical Electrochemical Workstation was used for the impedance and cyclic voltammetry measurements, and a Neware electrochemical testing system was used for the rest of the electrochemical measurements. For the galvanostatic cycling test of EG||Zn and EG||graphite cells, the cells were cycled at 100 and 200 mA g^{-1} . The cells were cycled between 0.2 and 2.5 V. The suspension electrolytes (x M $\text{Zn}(\text{OTf})_2$ in water/DMC, $x = 1, 2$ and 3) were used as the electrolyte. Either Zn



foil or a graphite negative electrode was used as the working electrode and the counter electrode. Electrochemical impedance spectroscopy (EIS) was performed at room temperature between 100 kHz and 0.1 Hz with an AC amplitude of 5 mV. EIS was also used to evaluate the apparent diffusion coefficient of anions.¹³

2.6 Calculations

Gaussian09 software was used to calculate the molecule configuration. The key words used were: # opt rb3lyp/6-31+g(d,p) scrf=(solvent=generic,read,pcm) gcom=connectivity field=x-50. The PCM continuum model was used to study the solvent effect. If the electric field needs to be removed, please delete the key word "field". The electronic density and configuration pictures were created using Multiwfn software.¹⁴

2.7 Simulations

The Tertiary Current Distribution module was applied to introduce the Nernst–Planck equation to describe the ion transport in COMSOL software, and the Electric Currents module was used to simulate the electric field distribution. More details can be seen in the "simulations" section in the ESI.†

3 Results and discussion

3.1 Formation, concept and physicochemical properties of SPSE

First, $\text{Zn}(\text{OTf})_2$ powder was added into the DMC solvent at the desired concentration and stirred thoroughly. Subsequently, a trace amount of water was added to adjust the anionic solvation structure. Trace amounts of water, capable of forming strong hydrogen bonds, were added based on a 1 : 1 molar ratio of H_2O to Zn^{2+} to finely tune the solvation structure of the particles. The molar quantity of water was calculated based on the mass or volume added, the density of water (1 g mL^{-1}), and the molar mass of water (18 g mol^{-1}). For example, 2 mol L^{-1} (M) $\text{Zn}(\text{OTf})_2$ in DMC was prepared, followed by the addition of $30 \mu\text{L mL}^{-1}$ of water to adjust the solvation structure and form SPSE. To clarify further, the notation $x \text{ M-SPSE-}y$ was used to represent different samples, where $x = 1, 2$, or 3 corresponds to the concentration, and $y = 15, 30$, or $45 \mu\text{L}$ represents the volume of water added. Note that the unit " mL^{-1} " is omitted in the symbols for simplicity. Accordingly, the samples 1 M-SPSE-15 μL , 2 M-SPSE-30 μL , and 3 M-SPSE-45 μL were prepared for comparison. $\text{Zn}(\text{OTf})_2$ was dissolved in DMC to obtain a clear and transparent saturated solution ($\leq 0.2 \text{ M}$). When the concentration of the salt in the electrolyte exceeded 1 M, most $\text{Zn}(\text{OTf})_2$ particles became insoluble, and a trace amount of water was added to optimize the solvation structure to form the final SPSE (Fig. 1A). Optical photographs of both the SPSE and the saturated $\text{Zn}(\text{OTf})_2$ based electrolyte are also shown. The linear carbonate DMC was mixed with low-dielectric aqueous electrolytes¹⁵ to guarantee high fluidity of the entire solution in the presence of high-concentration particles. In DIBs, the graphite cathode does not contain active anions, and the initial

concentration of anions remains fixed. The electrolyte plays a crucial role in DIBs as it serves as the source of both anions and cations. Thus, the concentration polarization primarily depends on anion diffusion at the cathode interface in DIBs, as anions serve as the main charge carriers. During energy storage, anions are continuously consumed through intercalation/de-intercalation to/from the electrodes or *via* side reactions. This consumption results in a decrease in anion concentration and the formation of a significant concentration gradient near the electrode surface, which can lead to performance issues. The SPSE design helps mitigate these effects by dynamically replenishing anions and reducing concentration gradients. Our study demonstrates that the use of a suspension electrolyte effectively enhances battery performance.

The following conditions need to be satisfied during the SPSE preparation to achieve the desired properties and appropriate combinations of main salts and organic solvents in the electrolyte: (i) the main salts need to be only slightly soluble in the organic solvents; (ii) a substantial excess of main salt particles should not result in a significant increase in viscosity; (iii) the SPSE should not solidify due to long-term standing at room temperature, while maintaining a microscopic phase separation between the particles and solvent. A key distinction of SPSE from conventional electrolytes lies in its ability to maintain high interfacial anion concentrations while preserving fluidity. Unlike liquid electrolytes that rely on fully dissolved salts,¹¹ gel electrolytes with constrained ion mobility,¹⁶ or other type electrolytes that lack dynamic anion replenishment,^{17,18} SPSE leverages the controlled micro-solubility of $\text{Zn}(\text{OTf})_2$ in a trace-water DMC solvent. This unique design mitigates concentration polarization, enhances anion utilization efficiency, and circumvents the cost and viscosity constraints associated with highly concentrated electrolytes. These key advantages circumvent the cost and viscosity challenges of high-concentration systems while addressing the anion depletion issues in existing DIB electrolytes.

To study the influence of salt concentration on the resistance of the SPSEs, four control electrolytes were prepared simultaneously, including a saturated electrolyte solution and 1 M, 2 M and 3 M SPSEs. The electrolytes were investigated by electrochemical impedance spectroscopy (EIS) under open circuit potential using expanded graphite||Zn (EG||Zn) cells, as shown in Fig. 1B. The 2 M-SPSE-30 μL had the lowest impedance and the highest ion diffusion coefficient, approximately $6.68 \times 10^{-12} \text{ cm}^2 \text{ s}^{-1}$ (Fig. 1C). For comparison, even though the 2 M-SPSE without water was used to measure impedance, a large semi-circle-shaped Nyquist plot is observed in Fig. S1.† The transference numbers of the EG||EG symmetric batteries using a saturated electrolyte solution and 2 M-SPSE-30 μL were measured, and the SPSE exhibited a higher value, indicating a greater anion contribution to the ionic current in SPSE (see more details in Fig. S2†). These properties are essential for optimizing the internal resistance and cycle performance of the battery.

Through Raman spectroscopy analysis, we explored the surface characteristics of solvated suspension particles in different solvents, which include pure DMC and a water/DMC



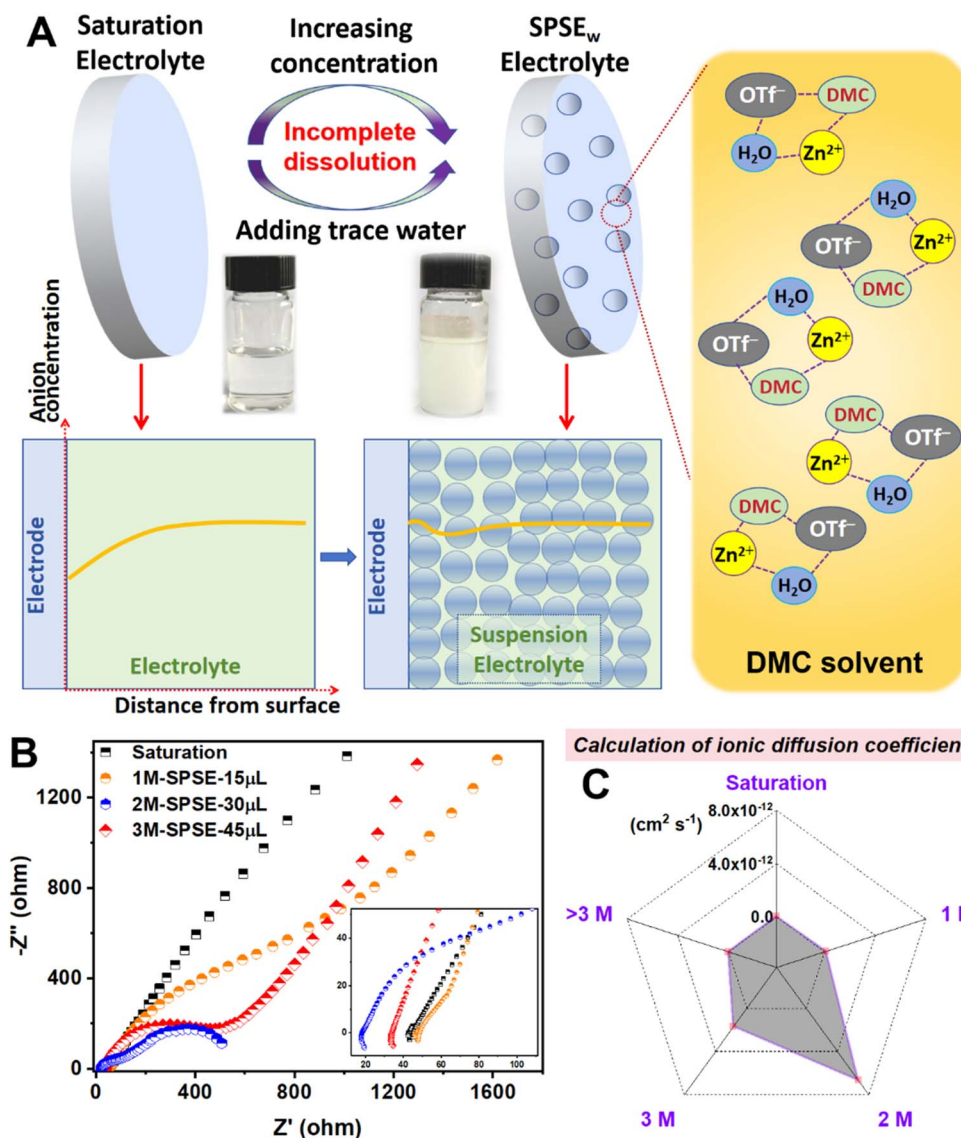


Fig. 1 (A) Scheme of the saturated electrolyte and SPSEs with a trace amount of water according to the molar amount of Zn^{2+} , depicting the chemical composition and the concentration profiles at the electrode interface, which allows reducing the concentration polarization in SPSE; (B) Nyquist plots and (C) corresponding ionic diffusion coefficients of EG||Zn cells using the electrolytes of 1 M-SPSE-15 μL , 2 M-SPSE-30 μL , and 3 M-SPSE-45 μL .

solution with the component ratio based on the sample of 2 M-SPSE-30 μL . Fig. 2A compares the spectra of eight samples, which include pure deionized water, a $\text{Zn}(\text{OTf})_2$ powder, various solvents, and the naturally air-dried $\text{Zn}(\text{OTf})_2$ powder. The liquid samples were fully filled in a highly transparent glass capillary tube for the measurements. The results showed the characteristic Raman peaks for pure water in the range of 3200–3800 cm^{-1} (Fig. S3†).^{19,20} The peak at 1035 cm^{-1} represents the $-\text{SO}_3$ group²¹ in $\text{Zn}(\text{OTf})_2$. Interestingly, the Raman spectrum of $\text{Zn}(\text{OTf})_2$ powder underwent significant changes upon the addition of the solvent, demonstrating a modification of the chemical environment and bonding among the ions and solvents in the electrolytes. In particular, the Raman peak at 1088 cm^{-1} significantly intensified, indicating the presence of free OTf^- anions.^{22,23} The introduction of water further

enhanced the Raman OTf^- peak intensity. After the removal of the solvent and subsequent air-drying of the suspended particles, the characteristic Raman peaks of the solid $\text{Zn}(\text{OTf})_2$ powder could be restored. However, the peaks attributed to the free OTf^- anions did not completely disappear after air-drying, indicating that the solvation structure was still partially retained.

Molecular mechanics calculations were employed to obtain the specific solvation structures. The software utilized was Chem3D, with the MM2 method being applied. Initially, a model was set up with a large number of $\text{Zn}(\text{OTf})_2$ molecules mixed with DMC molecules. The results indicated that each $\text{Zn}(\text{OTf})_2$ molecule interacted strongly with only one DMC molecule. Therefore, the structure and charge distribution of $\text{Zn}(\text{OTf})_2$ molecules and their binding with one or two DMC

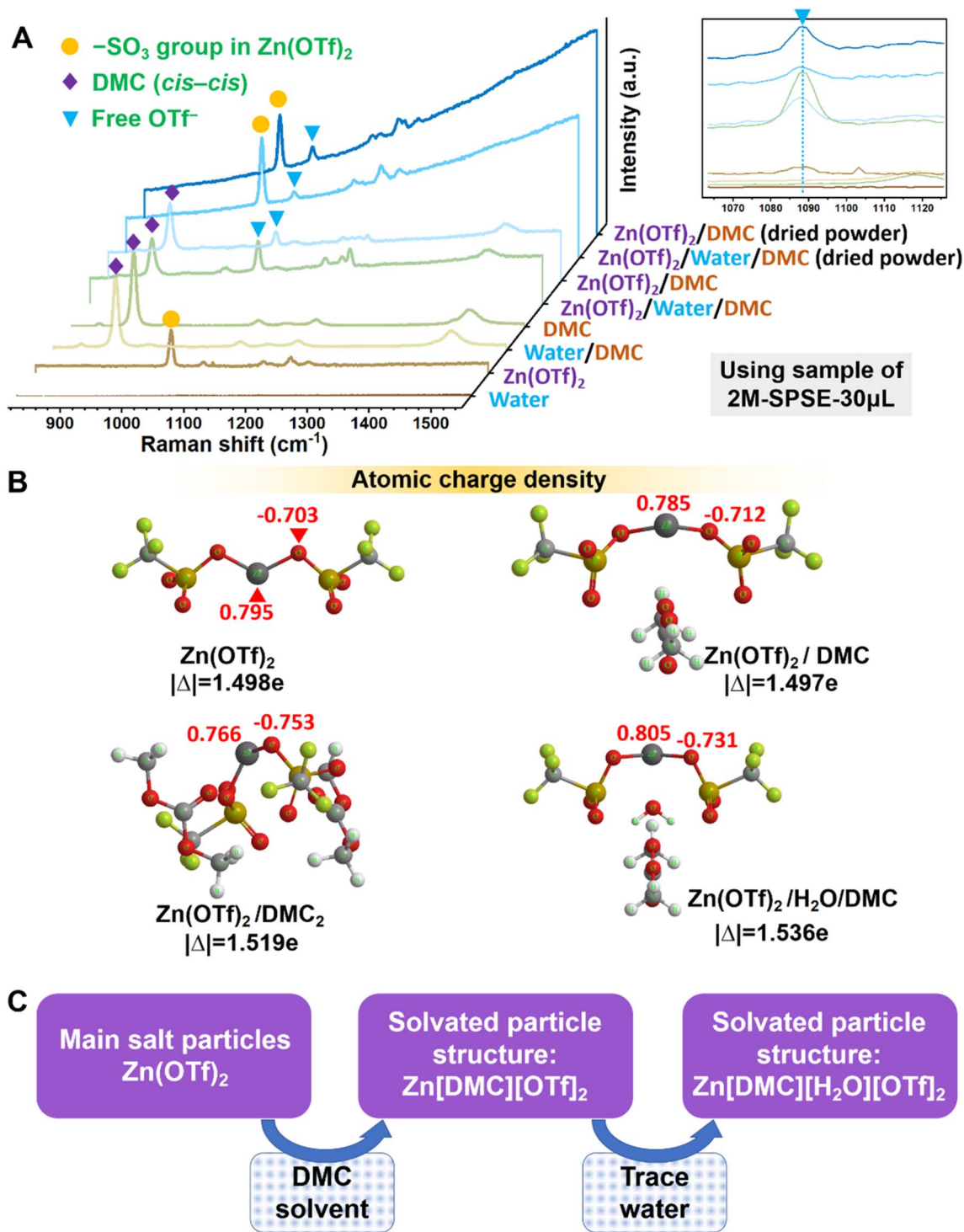


Fig. 2 (A) Raman spectra of samples, including water liquid, $\text{Zn}(\text{OTf})_2$ powder, water/DMC liquid, DMC liquid, $\text{Zn}(\text{OTf})_2$ in water/DMC solution (2 M), $\text{Zn}(\text{OTf})_2$ in DMC solution (2 M), air-dried $\text{Zn}(\text{OTf})_2$ powder from $\text{Zn}(\text{OTf})_2$ in water/DMC solution, and air-dried $\text{Zn}(\text{OTf})_2$ powder from $\text{Zn}(\text{OTf})_2$ in DMC solution; all the component ratios are based on the sample of 2 M-SPSE-30 μL ; (B) molecular mechanics calculations for the $\text{Zn}(\text{OTf})_2$, $\text{Zn}(\text{OTf})_2/\text{DMC}$, $\text{Zn}(\text{OTf})_2/\text{DMC}_2$ and $\text{Zn}(\text{OTf})_2/\text{H}_2\text{O}/\text{DMC}$ molecules, and the calculation of atomic charge distribution results using the extended Hückel method (the symbol $|\Delta|$: the absolute value of the charge difference between the Zn atom and the neighboring ether O atom); (C) diagram showing the formation procedure of solvated main salt particles.

were further computed and compared. As depicted in Fig. 2B, the charge difference (defined as $|\Delta|$ in the figures) of the Zn–O bond suggested that a single DMC molecule has a minimal

dissociation effect on $\text{Zn}(\text{OTf})_2$. However, upon the addition of two DMC molecules, the charge difference increases, indicating that the main salt is more prone to dissociation.^{24,25} After the



addition of trace amounts of water, the calculations showed that water molecules replaced one of the DMC molecules, resulting in a structure where the $\text{Zn}(\text{OTf})_2$ molecule interacted strongly with one DMC molecule and one water molecule. Consequently, the charge difference was further enhanced after the addition of water. This is beneficial for the desolvation and intercalation of anions.

Combining the results of Raman spectroscopy and molecular mechanics calculations, it is concluded that the addition of DMC did not alter the spectral characteristics of the main salt itself in the SPSE but enhanced the peak intensity of the free OTf^- anion. This indicates an interaction between DMC and $\text{Zn}(\text{OTf})_2$ and the formation of the $\text{Zn}[\text{DMC}][\text{OTf}]_2$ complex. The introduction of water further enhanced the OTf^- peak intensity, leading to the formation of $\text{Zn}[\text{DMC}][\text{H}_2\text{O}][\text{OTf}]_2$. Fig. 2C illustrates the solvation process of the suspension particles during the formation of SPSE, as derived from the aforementioned analysis.

3.2 Assembling and testing the dual-ion batteries

A prototype of graphite||Zn DIBs utilizing the freshly prepared SPSEs was assembled and tested. During battery assembly, EG was used as the positive electrode, zinc foil served as the negative electrode, and an SPSE was used on both sides of the aqueous separator. As illustrated in Fig. 3A, the cross-section of the cell core extracted from the assembled battery revealed a distinctive macroscopic state of the electrolyte, resembling a semi-solid state of matter.

Scanning electron microscopy (SEM) images showcased the morphology of EG before and after battery assembly. The stainless steel mesh current collector was covered with an EG layer and a conductive network consisting of Super P particles (Fig. 3B and C). EG presented a flake-like structure with dimensions less than 10 micrometers. On disassembled and air-dried electrodes, the surface of EG formed a loose porous

solvated $\text{Zn}(\text{OTf})_2$ coating composed of micro/nanoflakes, resembling flowers (Fig. 3D), which aided in ion transport and electrode protection.

The influence of different water contents in 2 M $\text{Zn}(\text{OTf})_2$ in DMC on the performance of the EG||Zn battery was investigated. Due to the hygroscopic nature of $\text{Zn}(\text{OTf})_2$ upon prolonged exposure to air (Fig. S4†), it was necessary to use freshly opened reagents and store them under vacuum. The GCD curves of the battery for the first two cycles are shown in Fig. 4A–C. Upon adding trace amounts of water, 10 or 20 $\mu\text{L mL}^{-1}$, significantly extended charging plateaus were observed in the low potential region below 1.7 V in the discharge curves. The plateaus, however, were short-lived, suggesting that the anion's desolvation effect is not significant at high potentials above 2.0 V, possibly due to the lower degree of dissociation of the main salt in the electrolyte. The discharge plateaus gradually shifted to higher potentials (≥ 2.0 V) with increased trace water content. They also covered longer discharge times, indicating an improvement in battery performance, including IR drop and coulombic efficiency (Fig. S5†). However, excessive water led to water decomposition on the positive electrode. The charge–discharge curves for the electrolytes with no water and excess water are shown in Fig. S6†.

Fig. 4D illustrates the initial charge/discharge curves for batteries with various samples of 1 M-SPSE-15 μL , 2 M-SPSE-30 μL and 3 M-SPSE-45 μL . The results show that the SPSE concentration significantly influences the battery's electrochemical reactions and performance. It was observed that the saturated electrolyte could not power the batteries due to a lack of active anions, as can be seen in the cyclic voltammetry curves (Fig. S7†). During the first cycle, charging plateaus above 2.2 V and discharge plateaus near 2.0 V were observed, which are notably higher than those (vs., Zn^{2+}/Zn) in standard aqueous batteries.^{26,27} In all EG||Zn cells with the three different SPSEs, very short discharge plateaus near 1.5–1.6 V were noted, aligning with the CV curves (refer to Fig. S8 in the ESI† for further

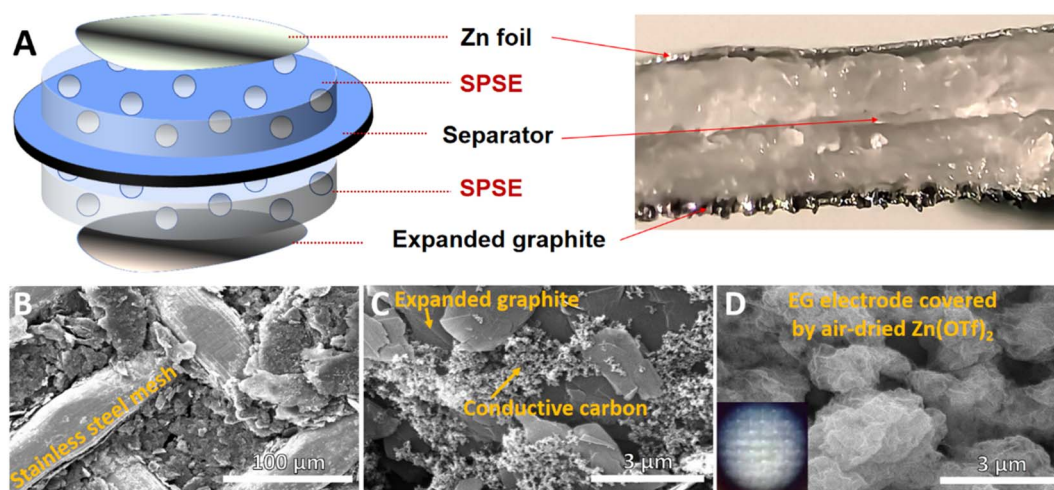


Fig. 3 (A) Scheme of the structure of an assembled EG||Zn battery and its real cross-sectional optical photograph; SEM images of the pristine expanded graphite electrode at (B) low and (C) high magnifications; (D) SEM image of the EG electrode covered with air-dried $\text{Zn}(\text{OTf})_2$ from the de-assembled cell (inset: an optical microscopy photograph of EG electrode covered with 2 M-SPSE-30 μL).



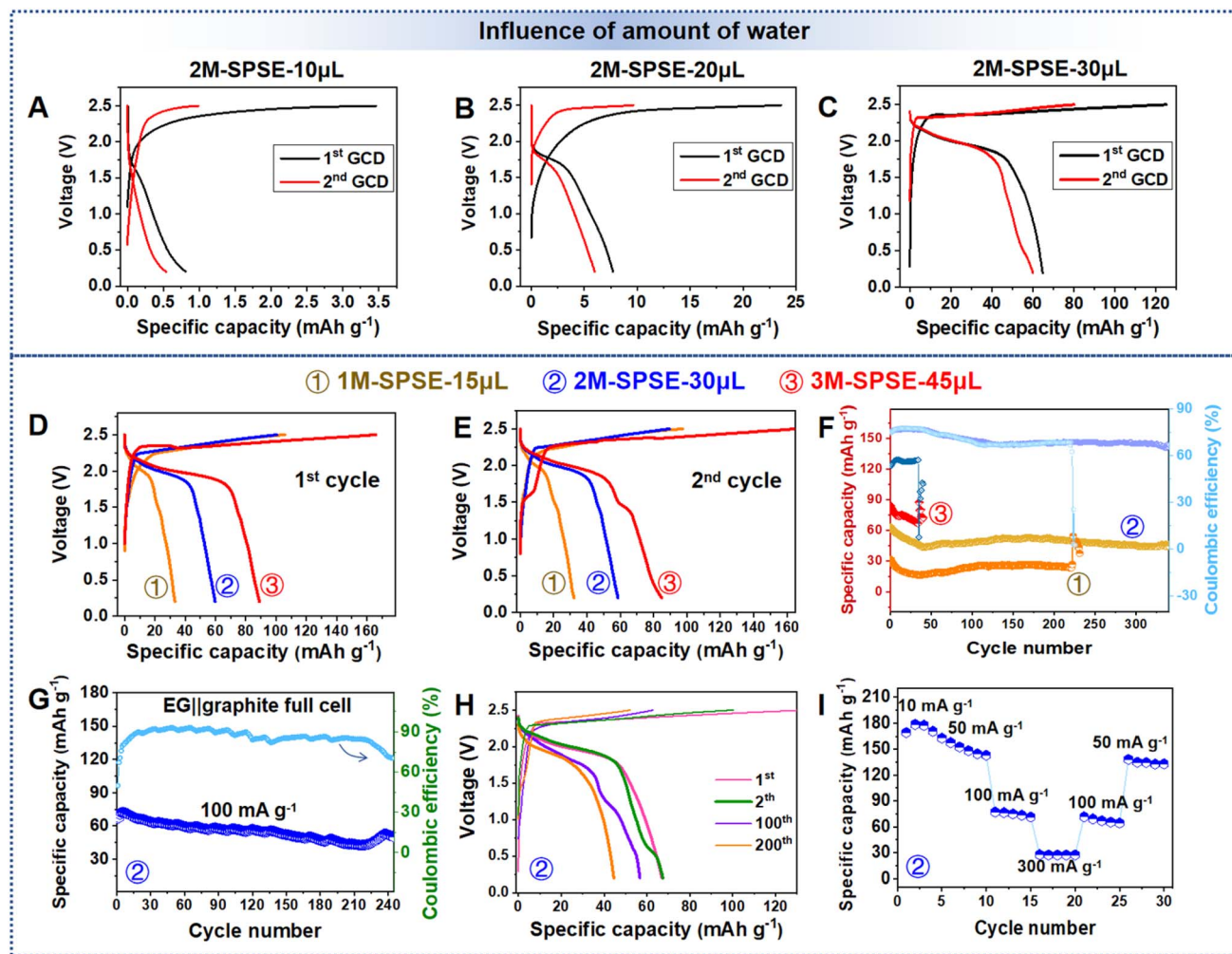


Fig. 4 The galvanostatic charge–discharge (GCD) curves (1st and 2nd cycles) of the EG||Zn cells using 2 M suspension electrolyte with different trace water contents of (A) 10 $\mu\text{L mL}^{-1}$ (2 M-SPSE-10 μL), (B) 20 $\mu\text{L mL}^{-1}$ (2 M-SPSE-20 μL) and (C) 30 $\mu\text{L mL}^{-1}$ (2 M-SPSE-30 μL) at 100 mA g^{-1} ; (D) the first and (E) second cycles of EG||Zn cells using the three electrolyte samples; (F) cycling performance of the EG||Zn cells at 100 mA g^{-1} ; (G) galvanostatic cycling performance for the EG||graphite dual-ion cell using 2 M-SPSE-30 μL at 100 mA g^{-1} , and (H) corresponding charge–discharge curves of the 1st, 2nd, 100th, and 200th cycles during the cycling test; (I) rate performance of the EG||graphite dual-ion cell using 2 M-SPSE-30 μL .

analysis). The results show that the plateaus or redox behavior is attributed to the reversible oxidation/reduction of the surface carbon. The cell with 3 M-SPSE-45 μL showed a decline in specific capacity from the second cycle (Fig. 4E), accompanied by a reduction in the 2 V discharge plateaus. Meanwhile, the cell with 2 M-SPSE-30 μL maintained the high-voltage discharge plateaus more effectively. Cycling tests revealed that the 3 M-SPSE-45 μL cell experienced rapid capacity fade and a short cycle life, whereas the 1 M-SPSE-15 μL and 2 M-SPSE-30 μL electrolyte cells exhibited better stability (Fig. 4F). Consequently, the 2 M-SPSE-30 μL was identified as the optimal choice for the EG||Zn dual-ion cells.

Moreover, dual-graphite DIB cells based on a zinc metal-free anode concept were assembled and the cycling performances were tested. In the zinc metal-free batteries, the reaction mechanism occurring on the graphite anode can also be described as $\text{Zn}^{2+} + 2\text{e}^- \rightarrow \text{Zn}$. This is similar to the reaction

mechanism on the Zn metal anode (see the Zn||graphite half cell in Fig. S9†), with the difference that the graphite anode has a much lower density, a higher specific surface area, and more adsorption sites. All these aspects contribute positively to the increase in the total energy density of the battery. The results (Fig. 4G) demonstrated that the EG||graphite cell with 2 M-SPSE-30 μL exhibited good cycling stability for at least 240 cycles at 100 mA g^{-1} , retaining 84.7% and 66.6% of its initial capacity after 100 and 200 cycles, respectively, with an average coulombic efficiency of over 86%. The cell achieved the highest specific capacity of 72.28 mA h g^{-1} during cycling. The charge–discharge curves of the 1st, 2nd, 100th, and 200th cycles during the cycling test at 100 mA g^{-1} are shown in Fig. 4H, with the voltage plateaus remaining stable near 2 V throughout long-term cycling. The EG||graphite dual-ion cell also exhibited good rate performance (Fig. 4I), achieving specific capacities of 178.66, 157.72, 77.23, and 27.86 mA h g^{-1} at 10, 50, 100, and

300 mA g⁻¹, respectively. Moreover, the maximum energy density based on the cathode was 304.8 W h kg⁻¹. The electrochemical performances rival that of DIBs using pure organic electrolytes.^{28–32} A comparison of their performances is listed in Table S1.† When comparing cathode materials in zinc-based batteries, the SPSE-based EG||Zn DIB not only exhibits good specific capacity but also achieves a much higher discharge voltage plateau compared to other aqueous Zn/Zn-ion batteries. This combination of advantages positions it as a promising candidate for high-energy-density applications. It is important to note that the SPSE is also beneficial for the Zn foil anode. The symmetric Zn–Zn cell could stably run over 190 hours by using 2 M-SPSE-30 μL according to the overpotential stability test, as shown in Fig. S10.†

3.3 *In situ* and *ex situ* characterization

The charge and discharge processes in the DIBs were investigated *in situ* using a homemade transparent glass electrochemical cell and optical microscopy (Fig. 5A). The graphite electrode and zinc foil were sandwiched between two glass slides, with the central portion of the electrolyte observed under a 400× magnification lens. During charging, particularly in the central region, some suspension particles dissolved in the SPSE (Fig. 5B). Interestingly, the particles redeposited at the interface between EG and the electrolyte during discharge (Fig. 5C). This indicates that suspension particles did not impede liquid flow or hinder anion migration to the graphite surface. The suspension particles also compensated for ion concentration

variation in the electrolyte during the charging and discharging cycles, effectively replenishing the ions in the electrolyte and creating a protective coating on the electrode surface. The suspension particle coating on the electrodes helped to confine desorbed ions near the electrode, reducing anion diffusion distance and improving utilization efficiency.

To perform *in situ* Raman spectroscopy on the EG electrode, we assembled EG||Zn batteries using button-type cell casings with circular holes, utilizing the optimal 2 M-SPSE-30 μL electrolyte. Fig. 5D illustrates the evolution of the G graphite band during the first charge–discharge cycle using *in situ* Raman spectroscopy. The G peak of pristine graphite was located at 1580 cm⁻¹, representing characteristic sp² carbon atoms. During the charging process, the G peak gradually shifted to higher wavenumbers before reaching 2.5 V (up to 1588 cm⁻¹), and the G' peak began to appear around 1610 cm⁻¹, indicating charge transfer and an increase in the interlayer spacing of graphite caused by anion intercalation.^{33,34} During discharge, the G' peak significantly intensified and then gradually diminished until discharge completion. A three-dimensional view of the *in situ* Raman spectra (Fig. S11†) provided a clearer comparison of the relative intensities of the peaks. During the initial charging process, the background signal and all peak intensities in the Raman spectra were significantly enhanced due to the intercalation of anions into the graphite lattice, leading to electrode structure expansion, which was subsequently alleviated in the following cycles. This phenomenon of graphite electrode anion intercalation has been reported in the

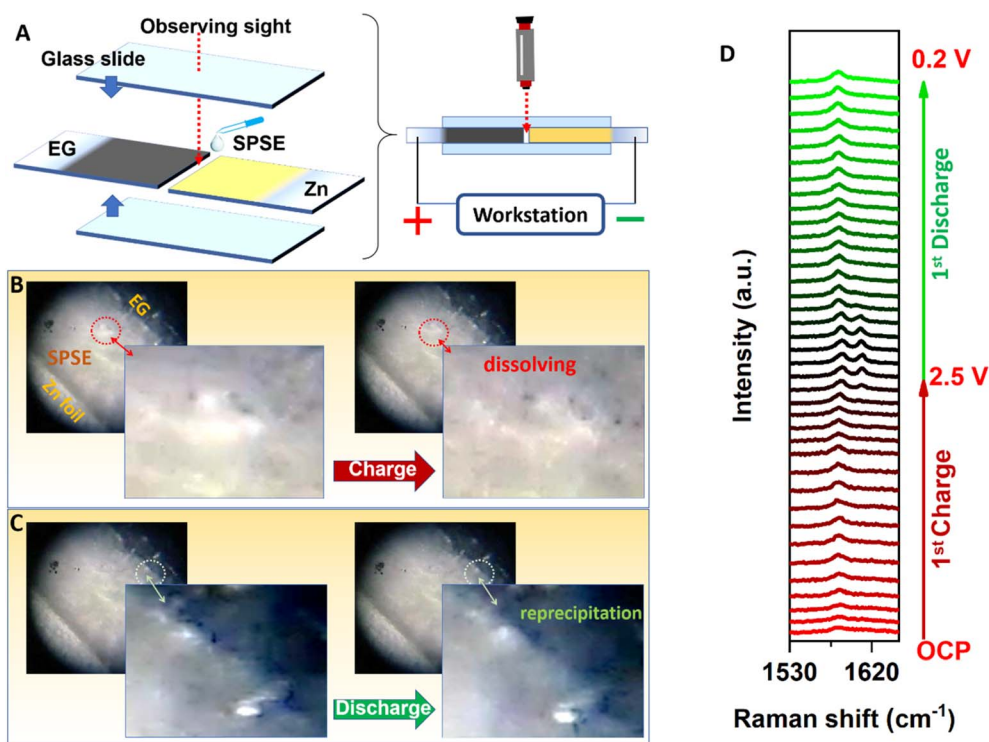


Fig. 5 (A) Scheme of the homemade glass cell for observing the changes in suspension particles during charge/discharge; corresponding photographs of the cell cross-sections in the (B) charge and (C) discharge states; (D) series of *in situ* Raman spectra from the first cycle (0.2–2.5 V) of the EG electrode in the EG||Zn cell using 2 M-SPSE-30 μL.

literature before.³⁵ Based on the behavior of these Raman peaks, graphite layers are reversibly intercalated and de-intercalated by OTf[−] anions, and the SPSE particles do not hinder the migration of anions to the electrode surface.

Ex situ XPS spectra were obtained for the pristine EG electrode and the EG electrodes after 10 cycles in different electrolyte concentrations, as shown in Fig. 6A. The C 1s spectrum indicated a sharp decrease in peak intensity following anion intercalation, with further weakening as the concentration increased, attributed to the coverage by the CEI. The O 1s spectra showed a low oxygen content in pristine graphite. The application of SPSEs (≥ 1 M) caused the O 1s peak to mainly appear near 533.3 eV, representing the S=O bond,^{36,37} which originated from the OTf[−] anion adsorbed on the graphite surface and intercalated between the graphite planes. The F 1s spectra mainly exhibited two peaks at 685.5 and 688.9 eV, representing ionic C_xF (4 < x < 20) and covalent C_xF (x ≤ 4),³⁸ respectively. The former enhancement is attributed to the intercalation of F atoms into the graphite lattice. The latter weakening, on the other hand, is due to the adsorption of undecomposed OTf[−] anions containing −CF₃ groups on the graphite surface. The intensity of the F 1s peak from ion intercalation reached its maximum value at 2 M electrolyte concentration. This indicates an optimal level of anion intercalation. The S 2p spectra revealed that the −SO₃[−] group could potentially convert into −SO₄ or SO₄^{2−}.^{39,40} The intensity of the peak representing C–S bonds at 163.0–163.2 eV (ref. 41) enhanced, most probably because of the presence of S^{2−} in the intercalated S-containing anions.⁴²

The compositions of the EG cathode surface at various charge/discharge states during the first cycle in 2 M-SPSE-30 μ L were also investigated by XPS (Fig. 6B). We selected samples at specific charge/discharge states (OCP \rightarrow 2 V \rightarrow 2.5 V \rightarrow 1.8 V \rightarrow 0.8 V) and analyzed how the chemical composition of the CEI on the surface of the EG cathodes changed during charging and discharging. The C 1s spectra showed two distinct peaks at

284.6 eV (sp² graphitized carbon) and 293.6 eV (−CF₃ group in OTf[−]) at open circuit potential (OCP). Both peaks increased upon charging up to 2.5 V and subsequently decreased during discharging to 0.8 V. The observed voltage variations in the −CF₃ peak intensity can be linked to variations in OTf[−] adsorption on the EG surface. The general trend in the intensity of the XPS peaks corresponds well to the expected intercalation/deintercalation states of the OTf[−] anions in the cathode as a function of voltage. However, an abnormal phenomenon is observed at 0.8 V, where the batteries are nearly fully discharged. At this voltage, the spectrum intensity unexpectedly increased. This could be attributed to the salt particle dissolution/precipitation process, which was previously observed by optical microscopy, shown in Fig. 5B and C. The adsorbed salt particles on the cathode acted as an ion-balancing CEI layer, which affected the concentration equilibrium of OTf[−] ions through particle swelling or dissolution, thus minimizing ion concentration excess/deficiency at the interface. The O 1s spectra also displayed a peak position recovery process that could be attributed to the migration of OTf[−] ions. The main oxygen peak shifted from 532.5 eV at OCP to 533.6 eV after charging to 2.5 V and subsequently returned back to the original position after discharging. This process can be associated with the formation and recovery of C=O (ref. 43 and 44) and C–O (ref. 45 and 46) bonds in the lattice. Interestingly, the F 1s spectra showed minimal changes at OCP and 2 V, with equal intensities of peaks attributed to the intercalated ionic C_xF and undecomposed −CF₃ groups. At 2.5 V, the ionic C_xF peak intensity remained high, while the −CF₃ peak diminished, indicating the desorption of OTf[−]. Similarly, the S 2p spectra exhibited varying peak intensities as a function of charge/discharge potential. Charging of the EG cathodes to 2.5 V enhanced the sulfur peak intensity, which then reversibly weakened after discharging, indicating anion intercalation and deintercalation in/from the graphite cathode. Overall, it can be concluded from the XPS results that the interface layer

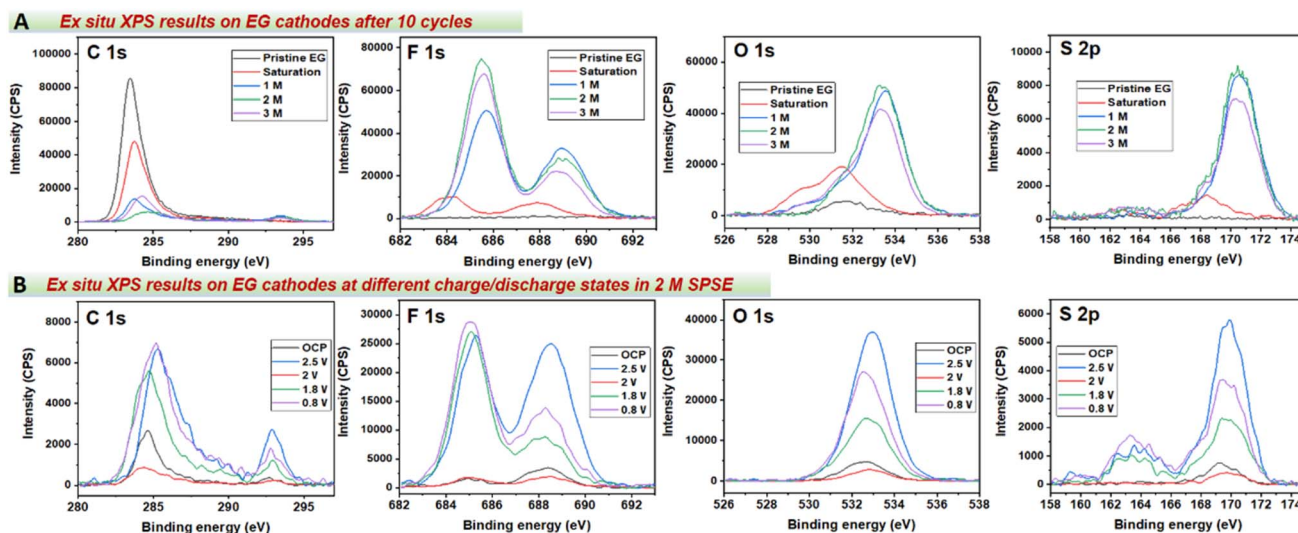


Fig. 6 (A) Comparison of *ex situ* XPS results of the pristine EG cathode and EG cathodes after 10 cycles in SPSEs of different concentrations; (B) comparison of *ex situ* XPS results of the EG cathodes at different charge/discharge states in 2 M-SPSE-30 μ L.



containing suspended particles acted directly as an efficient CEI layer on the graphite cathode. The interfacial salt particles provided excellent protective functionality, positively enhancing the intercalation and deintercalation of anions in/from the graphite cathode and mitigating concentration polarization at the electrolyte–electrode interface.

3.4 Simulations and calculations

The EIS results indicated a high diffusion impedance ($\geq 500 \Omega$) in SPSE under OCP; however, GCD tests revealed normal battery

charging and discharging with a high discharge plateau. This suggests that the suspension particles in SPSE undergo changes under the influence of the electric field, as explained by quantum mechanics calculations.

Through simulations using Gaussian09 software, we analyzed the solvation structure of $\text{Zn}(\text{OTf})_2$ molecules under the influence of an electric field. Fig. 7A displays the molecular configuration of $\text{Zn}(\text{OTf})_2$ and the corresponding electron density map under a $5.1 \text{ V } \text{\AA}^{-1}$ electric field, revealing that the electron density (created by Multiwfn¹⁴) is primarily

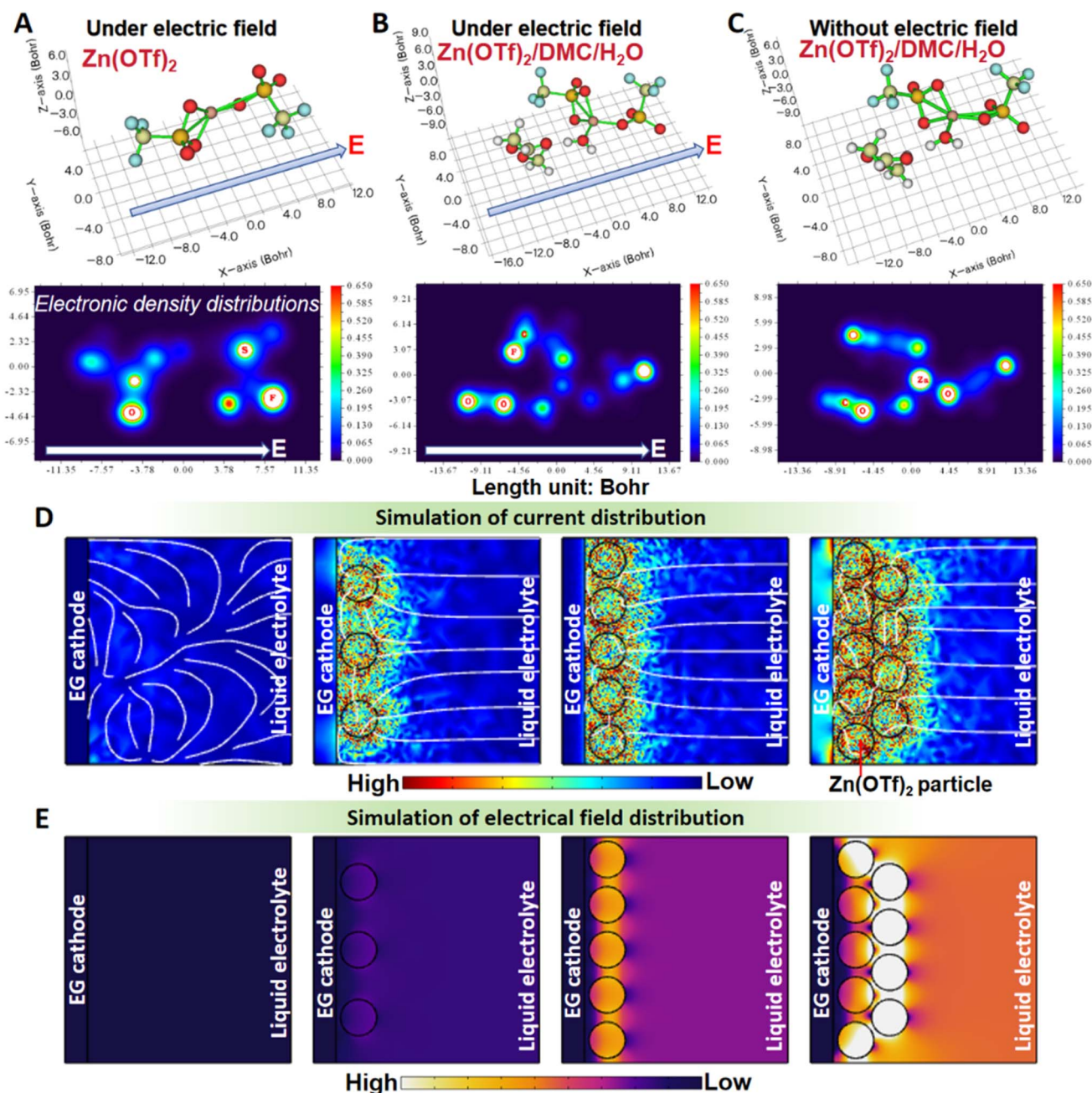


Fig. 7 Calculation results of the configurations for (A) single $\text{Zn}(\text{OTf})_2$ molecules under an electric field, (B) $\text{Zn}(\text{OTf})_2/\text{H}_2\text{O}/\text{DMC}$ molecules under an electric field, and (C) $\text{Zn}(\text{OTf})_2/\text{H}_2\text{O}/\text{DMC}$ molecules without an electric field; the electronic density results are listed in corresponding bottom pictures; simulation results of (D) current distribution and (E) electrical field distribution.



concentrated on the OTf[−] anion groups. When H₂O and DMC molecules are introduced into the simulated environment (Fig. 7B), considering the DMC solvent effect with a dielectric constant of 3.1,¹⁵ the electron density shifts towards DMC and adjacent OTf[−] groups, while the bond length between distant OTf[−] groups and Zn²⁺ increases, resulting in a decrease in electron density. In contrast, under no electric field conditions (Fig. 7C), the electron density is evenly distributed over DMC, water molecules, and Zn atoms. These results suggest that the electric field can promote the dissociation of suspended salt particles, potentially leading to particle dissolution. As analyzed earlier, the dissociated ions can migrate to the surface of the positive electrode and reform suspended particles after desorption, a process represented by the following reaction equation:



COMSOL software simulations clarified the localizing effect by modeling a large rectangle as the electrolytic cell, a slender rectangle as the graphite electrode, and circles representing suspension particles. The ionic current under galvanostatic conditions predominantly surrounded the suspension particles, with the current density increasing proportionally to the particle number (Fig. 7D). This correlation explains the link between higher particle concentration and greater specific capacity. The particles on the graphite surface were crucial for ionic current flow and served as the primary source of OTf[−] anions. Additionally, the electric field distribution (Fig. 7E) revealed that the particle network created a high-intensity shielding layer near the electrode, limiting anion migration to the bulk electrolyte during discharge and improving anion utilization efficiency. This localizing effect not only minimized anion loss on the graphite surface but also enabled swift ion replenishment. However, it should be noted that the proposed localizing effect is inferred from indirect evidence, including XPS analysis, optical microscopy observations, and theoretical simulations. While these results strongly suggest the dynamic evolution of anions at the interface, particularly at the closing interface (a spatially confined boundary between the electrode surface and suspended particles), this remains experimentally elusive due to its transient and nanoscale nature. Future studies employing advanced *in situ* techniques are necessary to directly probe the dynamic properties of this interface, and validate its role in stabilizing ion transport pathways.

The exceptional electrochemical performance in DIBs using SPSE is also due to other physical characteristics of the suspension particle layer on the EG cathode. The rich hydrogen bonding within the solvated structure creates a highly polar environment for the OTf[−]/DMC/H₂O complex. This configuration exhibits piezoelectric-like properties, as confirmed by specific tests (see Fig. S12 in the ESI† for detailed piezoelectricity analysis). Under assembly pressure, the cell with the SPSE showed a higher OCP, a behavior not observed with the clear saturated electrolyte. Additionally, this property promotes

anion accumulation near the EG cathode, mitigating concentration polarization.

4 Conclusions

In this study, by capitalizing on the low solubility of the main salt in DMC solvent with a low dielectric constant and the modulation of the solvation structure with a trace amount of water, we have successfully developed a 2 M solvated main salt particle suspension Zn(OTf)₂ electrolyte for DIBs. Compared to traditional electrolytes where the main salt is completely dissolved, the presence of a large number of undissolved solvated particles does not impede ion mobility but rather enables the electrolyte to achieve the functionality of a high-concentration electrolyte at a lower concentration. Furthermore, the SPSE can enhance the anion utilization efficiency at the electrode surface by significantly increasing the surface concentration and preventing the anions from migrating toward the bulk solution after de-intercalation. In zinc metal-anode free EG||graphite DIB cells, the SPSE achieved specific capacities of 178.66 and 77.23 mA h g^{−1} at current densities of 10 and 100 mA g^{−1}, respectively, with a high discharge platform of approximately 2.0 V. The SPSE holds promise for inspiring a new generation of electrolytes, facilitating the transition from liquid to semi-solid systems.

Data availability

The data supporting this article have been included as part of the ESI.†

Conflicts of interest

There are no conflicts to declare.

Acknowledgements

Y. He gratefully acknowledges the financial support from the National Natural Science Foundation of China (No. 52202200), and the Excellent Young Talents Fund Program of Higher Education Institutions of Anhui Province (No. 2022AH030048), and the financial support of the European Union and the Czech Ministry of Education, Youth and Sports (Project: MSCA Fellowships CZ FZU III – CZ.02.01.01/00/22_010/0008598). J. Červenka acknowledges the financial support by the Advanced Multiscale Materials for Key Enabling Technologies project (Project No. CZ.02.01.01/00/22_008/0004558), supported by the Czech Ministry of Education, Youth, and Sports and the European Union, and funding support from the Czech Science Foundation (GACR – Grant No. 24-10535K).

References

- 1 Y. T. He, Z. P. Chen and Y. H. Zhang, *iScience*, 2024, **27**, 110491.
- 2 Y. T. He, X. X. Shen and Y. H. Zhang, *ACS Appl. Nano Mater.*, 2024, **7**, 27907–27939.



- 3 Y. He, Y. Dong, Y. Zhang, Y. Li and H. Li, *Adv. Sci.*, 2023, **10**, e2207426.
- 4 B. Jiang, C. H. Zhao, X. J. Yin, Y. Zhang, X. Sun, S. Gu and N. Q. Zhang, *Energy Storage Mater.*, 2024, **66**, 103237.
- 5 L. J. Zhang, H. T. Wang, X. M. Zhang and Y. B. Tang, *Adv. Funct. Mater.*, 2021, **31**, 2010958.
- 6 L. Xiang, X. Ou, X. Wang, Z. Zhou, X. Li and Y. Tang, *Angew. Chem. Int. Ed. Engl.*, 2020, **59**, 17924–17930.
- 7 M. S. Kim, Z. Zhang, P. E. Rudnicki, Z. Yu, J. Wang, H. Wang, S. T. Oyakhire, Y. Chen, S. C. Kim, W. Zhang, D. T. Boyle, X. Kong, R. Xu, Z. Huang, W. Huang, S. F. Bent, L. W. Wang, J. Qin, Z. Bao and Y. Cui, *Nat. Mater.*, 2022, **21**, 445–454.
- 8 X. Ou, D. Gong, C. Han, Z. Liu and Y. Tang, *Adv. Energy Mater.*, 2021, **11**, 2102498.
- 9 S. Mubeen, Y. S. Jun, J. Lee and E. W. McFarland, *ACS Appl. Mater. Interfaces*, 2016, **8**, 1759–1765.
- 10 Z. Qi and G. M. Koenig, *J. Power Sources*, 2016, **323**, 97–106.
- 11 Y. Dong, L. Miao, G. Ma, S. Di, Y. Wang, L. Wang, J. Xu and N. Zhang, *Chem. Sci.*, 2021, **12**, 5843–5852.
- 12 Y. Zhang, X. Cao and P. Xiao, *J. Power Sources*, 2024, **590**, 233805.
- 13 Y. C. Liu, L. Z. Fan and L. F. Jiao, *J. Mater. Chem. A*, 2017, **5**, 1698–1705.
- 14 T. Lu and F. Chen, *J. Comput. Chem.*, 2012, **33**, 580–592.
- 15 J. Self, B. M. Wood, N. N. Rajput and K. A. Persson, *J. Phys. Chem. C*, 2018, **122**, 1990–1994.
- 16 C. Austen Angell, *Electrochim. Acta*, 2019, **313**, 205–210.
- 17 S. Nanda and A. Manthiram, *Adv. Energy Mater.*, 2021, **11**, 2003293.
- 18 T. Zhang, Y. Tang, S. Guo, X. Cao, A. Pan, G. Fang, J. Zhou and S. Liang, *Energy Environ. Sci.*, 2020, **13**, 4625–4665.
- 19 G. E. Walrafen, *J. Chem. Phys.*, 1964, **40**, 3249–3256.
- 20 D. M. Carey and G. M. Korenowski, *J. Chem. Phys.*, 1998, **108**, 2669–2675.
- 21 Y. Dong, N. Zhang, Z. D. Wang, J. H. Li, Y. X. Ni, H. L. Hu and F. Y. Cheng, *J. Energy Chem.*, 2023, **83**, 324–332.
- 22 P. Lin, G. Chen, Y. Kang, M. Zhang, J. Yang, Z. Lv, Y. Yang and J. Zhao, *ACS Nano*, 2023, **17**, 15492–15503.
- 23 C. A. Kruithof, A. Berger, H. P. Dijkstra, F. Soulimani, T. Visser, M. Lutz, A. L. Spek, R. J. Gebbink and G. van Koten, *Dalton Trans.*, 2009, 3306–3314.
- 24 B. Hribar, N. T. Southall, V. Vlasy and K. A. Dill, *J. Am. Chem. Soc.*, 2002, **124**, 12302–12311.
- 25 R. F. W. Bader, *Chem. Rev.*, 2002, **91**, 893–928.
- 26 Y. Liang and Y. Yao, *Nat. Rev. Mater.*, 2022, **8**, 109–122.
- 27 D. Chao, W. Zhou, F. Xie, C. Ye, H. Li, M. Jaroniec and S. Z. Qiao, *Sci. Adv.*, 2020, **6**, eaba4098.
- 28 W. Huang, B. Meng, J. Li, K. Yang and Z. Fang, *ACS Appl. Energy Mater.*, 2022, **5**, 14487–14495.
- 29 J. Li, C. Han, X. Ou and Y. Tang, *Angew. Chem., Int. Ed.*, 2022, **61**, e202116668.
- 30 J. Zhu, Y. Li, B. Yang, L. Liu, J. Li, X. Yan and D. He, *Small*, 2018, **14**, e1801836.
- 31 Z. Hu, Q. Liu, K. Zhang, L. Zhou, L. Li, M. Chen, Z. Tao, Y. M. Kang, L. Mai, S. L. Chou, J. Chen and S. X. Dou, *ACS Appl. Mater. Interfaces*, 2018, **10**, 35978–35983.
- 32 B. Pattavathi, V. Surendran, S. Palani and M. M. Shaijumon, *J. Energy Storage*, 2023, **68**, 107878.
- 33 D. C. Alsmeyer and R. L. McCreery, *Anal. Chem.*, 2002, **64**, 1528–1533.
- 34 M. Balabajew, H. Reinhardt, N. Bock, M. Duchardt, S. Kachel, N. Hampp and B. Roling, *Electrochim. Acta*, 2016, **211**, 679–688.
- 35 R. Yivlialin, G. Bussetti, L. Brambilla, C. Castiglioni, M. Tommasini, L. Duò, M. Passoni, M. Ghidelli, C. S. Casari and A. Li Bassi, *J. Phys. Chem. C*, 2017, **121**, 14246–14253.
- 36 C. L. Liu, T. Cao, Z. P. Wang, K. Li, Y. Gong and D. L. Zhang, *Electrochim. Acta*, 2022, **436**, 141447.
- 37 W. Yan, S. Chen, M. Wen, Q. Wu and S. Yu, *J. Mater. Chem. A*, 2021, **9**, 2276–2283.
- 38 J.-M. Lee, S. J. Kim, J. W. Kim, P. H. Kang, Y. C. Nho and Y.-S. Lee, *J. Ind. Eng. Chem.*, 2009, **15**, 66–71.
- 39 A. Fahmy, M. A. Kolmangadi, A. Schönhals and J. Friedrich, *Plasma Processes Polym.*, 2022, **19**, 2100222.
- 40 M. Ahmadian, M. Anbia and M. Rezaie, *Ind. Eng. Chem. Res.*, 2020, **59**, 21642–21653.
- 41 F.-L. Zeng, X.-Y. Zhou, N. Li, A.-B. Wang, W.-K. Wang, Z.-Q. Jin, Y.-R. Ren, B.-J. Fang, N.-Y. Yuan and J.-N. Ding, *Energy Storage Mater.*, 2021, **34**, 755–767.
- 42 S. De Rosa, P. Branchini, R. Yivlialin, L. Duò, G. Bussetti and L. Tortora, *ACS Appl. Nano Mater.*, 2019, **3**, 691–698.
- 43 X. Li, M. Xu, Y. Chen and B. L. Lucht, *J. Power Sources*, 2014, **248**, 1077–1084.
- 44 Z. Zhu, C. Liu, X. M. Song, Q. Mao and T. Ma, *ACS Appl. Bio Mater.*, 2021, **4**, 3623–3629.
- 45 Y. Lin, Z. Feng, L. Yu, Q. Gu, S. Wu and D. S. Su, *Chem. Commun.*, 2017, **53**, 4834–4837.
- 46 H. D. Pham, M. Horn, J. F. S. Fernando, R. Patil, M. Phadatare, D. Golberg, H. Olin and D. P. Dubal, *Sustainable Mater. Technol.*, 2020, **26**, e00230.

